



# Modelling and analysis of the oxidation influence on creep behaviour of thin-walled structures of the single-crystal nickel-base superalloy René N5 at 980 °C

Matthias Bensch<sup>a</sup>, Johannes Preußner<sup>a</sup>, Rainer Hüttner<sup>a</sup>, Georgia Obigodi<sup>b</sup>,  
Sannakaisa Virtanen<sup>b</sup>, Johannes Gabel<sup>c</sup>, Uwe Glatzel<sup>a,\*</sup>

<sup>a</sup> *Metals and Alloys, University Bayreuth, Ludwig-Thoma-Str. 36b, 95447 Bayreuth, Germany*

<sup>b</sup> *Dept. for Materials Science and Engineering, WW4-LKO, University of Erlangen-Nuremberg, Martensstr. 7, 91058 Erlangen, Germany*

<sup>c</sup> *MTU Aero Engines, Dachauer Str. 665, 80995 Munich, Germany*

Received 28 August 2009; received in revised form 30 October 2009; accepted 3 November 2009

## Abstract

Creep test results of thin-walled specimens of the single-crystal nickel-base superalloy René N5 at 980 °C under vacuum as well as under air show different creep properties depending on material thickness and atmosphere. The differences in creep strength and strain were analysed based on a creep-oxidation model. The model specifies the primary and secondary creep stages of thin-walled specimens by a sequence of layers. The model takes different zones affected by oxidation into account. Four layers were experimentally observed and considered in the model: oxide layer,  $\gamma'$ -free layer,  $\gamma'$ -reduced layer and the two-phase substrate in the sample as centre. Material parameters for growth laws of each layer were identified both by experimental analyses and by thermodynamic simulations. The final creep-oxidation model characterizes the creep behaviour of samples with small thicknesses and low initial stress with high accuracy.

© 2009 Acta Materialia Inc. Published by Elsevier Ltd. All rights reserved.

*Keywords:* Creep; Oxidation; Modelling; Thin-walled structures; Nickel alloy

## 1. Introduction

Creep deformation restricts the operating time of single-crystal nickel-base superalloys used in turbine blades of gas turbines and aeroplane engines [1]. A reduction of the wall thickness of turbine blades not only allows the weight of the component to be reduced, it also can raise the cooling efficiency of the blades. However, oxidation effects play a decisive role for the creep strength of blades with reduced wall thickness. Oxidation is the main effect of corrosion at temperatures above 950 °C [2]. The application of high-temperature alloys, like René N5, depends on the ability of the material to create protective, dense and slow-growing oxide layers, with a low defect density [3].

Dryepontd et al. [4] examined the coupling between creep behaviour and oxidation for the single-crystal superalloy MC2 at 1150 °C. They highlight that the formation of a non-load-bearing zone does not completely account for the big difference in creep rate between tests performed under synthetic air and under hydrogenated argon.

Doner and Heckler [5,6] analysed the uncoated nickel-base superalloy CMSX-3 at 982 °C at stress levels of 275 MPa and below. Reducing the wall thickness from 3.18 to 0.76 mm, they observed a loss in creep rupture life of 30% and that the time to reach 1% strain is unaffected by wall thickness at a constant stress level.

Seetharaman et al. [7] found similar results with the single-crystal superalloy PWA 1484 and wall thicknesses between 1.76 and 0.38 mm at 982 °C and stresses of 275 MPa and below. They concluded that oxidation and constrained plastic deformation are the major contributions for early failure of thin samples.

\* Corresponding author. Tel.: +49 921 55 5555; fax: +49 921 55 5561.  
E-mail address: [uwe.glatzel@uni-bayreuth.de](mailto:uwe.glatzel@uni-bayreuth.de) (U. Glatzel).

Hüttner et al. [8,9] studied the creep behaviour of [0 0 1] orientated thin-walled single-crystal René N5 samples at 980 °C under a constant load and initial stresses of 230, 270 and 300 MPa. The uncoated specimens show that a reduction in wall thickness from 1.0 to 0.3 mm leads to lower creep rupture strains, lower lifetimes and higher minimum creep strain rates.

The aim of the present paper is to both model and investigate the influence of oxidation on creep behaviour of uncoated and thin-walled structures in order to understand the influence of wall thickness and oxidation on creep behaviour. Thereby it should be possible to predict the creep behaviour. The essential parameters and relations for the model are identified using experiments as well as thermodynamic and kinetic simulations.

## 2. Materials and experimental procedures

For the creep tests, a cast and standard heat-treated [8,9] single-crystal plate of René N5 (Table 1) was provided by MTU Aero Engines, Munich. The plate, which was orientated by Laue back-scattered diffraction in [0 0 1] orientation, was cut by wire electrical discharge machining. Two specimen series (geometries  $95 \times 3 \times 1 \text{ mm}^3$  and  $95 \times 4 \times 0.3 \text{ mm}^3$ ) were cut from the [0 0 1] oriented slice. The creep tests were performed until rupture of the samples at constant load and temperature of 980 °C for three initial stress levels of 230, 270 and 300 MPa [8,9]. The tests were performed in both air and vacuum. The creep test results under vacuum and air are necessary for the determination of the model constants.

Furthermore, oxidation tests of thin René N5 samples, with the same orientation and geometries as the creep specimens, were carried out. The oxidation samples were prepared by cutting untested creep specimens. Cross-sections of the oxidized samples were mechanically polished with SiC paper and diamond paste down to 1  $\mu\text{m}$ . To investigate the  $\gamma'$  phase the quadrant back-scattering detector (QBSD) in a Zeiss 1540 EsB scanning electron microscope (SEM) was used. The oxidation tests are performed to investigate the growth law of each layer in stress-free conditions. By this way spallation caused by elongation of the sample during creep is prevented.

Thin sheets are heat-treated in air for different times, from 0 h to 100 h. Samples were analysed more frequently within the first 2 h, in order to provide a good time resolution at the onset of oxidation.

Moreover, thermodynamic simulations with ThermoCalc [11] and kinetic simulations with DICTRA [12] were performed to identify the growth law of the  $\gamma'$ -reduced

layer thickness and to verify the experimental results of the oxidation tests.

## 3. Theoretical approach

The technically important primary and secondary creep stages are included in the material model. Tertiary creep is not considered in this work.

The primary and secondary creep stages are approximated by the Garofalo equation [13,14]. In this time-dependent equation,  $\varepsilon_0$  describes the instantaneous strain on loading,  $\varepsilon_t$  the limit for transient creep,  $\dot{\varepsilon}_s$  the steady-state creep rate in the secondary creep region and  $m$  the ratio of transient creep rate to the transient creep strain:

$$\varepsilon = \varepsilon_0 + \varepsilon_t(1 - e^{-m \cdot t}) + \dot{\varepsilon}_s \cdot t \quad (1)$$

Because the measurement of the strain in the conducted creep tests [8,9] starts after loading the sample, the elastic strain  $\varepsilon_0$  is neglected.

Fig. 1 shows a schematic drawing of stacked layers evolving during oxidation. The actual creep specimens have the dimensions:  $95 \times 3 \times 1 \text{ mm}^3$  or  $95 \times 4 \times 0.3 \text{ mm}^3$  [8]. Before the creep test the structure consists entirely of the single-crystal nickel-base superalloy with cuboidal  $\gamma'$  precipitates, which are embedded in a  $\gamma$  Ni solid solution matrix. The time interval of the test is  $\Delta t$ . The creep-oxidation model uses the sequence of layers with different creep properties. The layers are infinitely large in two dimensions and symmetric to the mirror plane in the centre of the sample.

Because length and width of the sample are very large in comparison to the sample thickness, a unit surface area  $A$  is used. The specimen thickness during oxidation exposure is denoted as  $l(t)$ . The initial thickness  $l_0 = l(t=0)$  can be written as a sum of layers (2):

$$l_0 = 2 \cdot (l_{\text{two-phase}} + l_{\gamma' \text{ red.}} + l_{\gamma' \text{ free}} + l_{\text{ox. inner}}) \quad (2)$$

The unaltered centre part of the sample is followed by a layer with reduced  $\gamma'$  volume fraction. The two exterior layers represent the  $\gamma'$ -free layer, also called Al-depleted zone, and finally the oxide layer. This oxide layer may consist of different isolated oxides. The width of the  $\gamma'$ -reduced layer is labelled with  $l_{\gamma' \text{ red.}}$  and the  $\gamma'$ -free layer with  $l_{\gamma' \text{ free}}$ . A SEM image of an oxidized sample is shown in Fig. 2.

In general, the oxide layer can be formed as an additional layer and can grow simultaneously into the substrate. The oxide layer total thickness is denoted as  $l_{\text{ox. total}}$ . The thickness of the part of the oxide layer moving inwards is denoted as  $l_{\text{ox. inner}}$ .

Table 1  
Nominal composition of René N5 and compositions used for DICTRA simulations (wt.%).

	Cr	Co	Mo	W	Ta	Re	Al	Hf	Ni	Source
Nominal composition of René N5	7	8	2	5	7	3	6.2	0.2	Bal.	[10]
Composition used for DICTRA simulation (Section 4.2.)	7	–	2	5	7	3	6.2	–	69.8	–
$\gamma'$ -free layer composition used for DICTRA simulation (Section 4.3.)	9.1	11.3	2.2	4.9	6.8	10.5	2.2	0.2	52.8	Measured by EDX

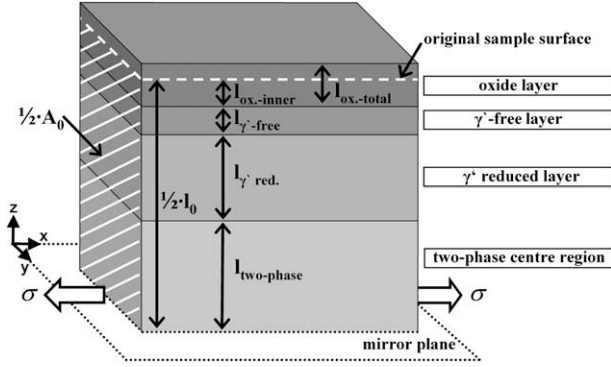


Fig. 1. Cross-sectional cut of a  $x$  and  $y$  direction infinitely extended thin-walled structure. A stack of layers is shown, which is symmetric to the indicated mirror plane. The bright layer in the centre represents the two-phase centre region. The subsequent layers are the  $\gamma'$ -reduced layer, the  $\gamma'$ -free layer and the oxide layer. The original thickness is  $l_0 = l(t = 0)$ .

The oxide layer  $l_{ox-total}$  is assumed to have no creep resistance. The reduction of the load-bearing cross-section through oxidation,  $l_0 - 2 \cdot l_{ox-inner}(t)$ , is used as creep resistant in the model. The thickness change of the load-bearing profile can be written as:

$$l(t) = l_0 - 2 \cdot l_{ox-inner}(t); \quad (3)$$

$$\begin{aligned} \sigma_{\gamma'-free} &= \frac{\sigma \cdot l_0 - \sigma_{two-phase} \cdot (l(t) - 2l_{\gamma' red.}(t) - 2l_{\gamma'-free}(t)) - \sigma_{\gamma' red.}(2l_{\gamma' red.}(t))}{2l_{\gamma' f}(t)} \\ &= \frac{\sigma \cdot l_0 - \left( \frac{A_{\gamma'-free}}{A_{two-phase}} \cdot \sigma_{\gamma'-free}^{n_{\gamma'-free}} \right)^{-n_{two-phase}} \cdot (l(t) - 2l_{\gamma' red.}(t) - 2l_{\gamma'-free}(t)) - \left( \frac{A_{\gamma' red.}}{A_{\gamma' red.}} \cdot \sigma_{\gamma' red.}^{n_{\gamma' red.}} \right)^{-n_{\gamma' red.}} \cdot 2l_{\gamma' red.}(t)}{2l_{\gamma'-free}(t)}; \end{aligned} \quad (9)$$

The creep properties of the other three layers,  $l_{two-phase}$ ,  $l_{\gamma'-free}$  and  $l_{\gamma' red.}$ , in their isothermal stationary creep stage, are described by the Norton creep law [17].

$$\dot{\varepsilon}_{s_j} = A_j \cdot \sigma_j^{n_j}; \quad (4)$$

$\dot{\varepsilon}_{s_j}$  indicates the steady-state creep rate influences  $\dot{\varepsilon}_s$  in Eq. (1),  $A_j$  a material-dependent constant,  $\sigma_j$  the stress acting on this layer and  $n_j$  the Norton creep exponent. The creep behaviour of the two-phase centre region ( $j = two-phase$ ), the  $\gamma'$ -reduced layer ( $j = \gamma' red.$ ) and the  $\gamma'$ -free layer ( $j = \gamma'-free$ ) are used.

One boundary condition is that the strain  $\varepsilon_{xx}$  is equal for all layers. For each layer (two-phase centre region,  $\gamma'$ -reduced layer and  $\gamma'$ -free layer) the material constants  $A_{two-phase}$ ,  $n_{two-phase}$ ,  $A_{\gamma' red.}$ ,  $n_{\gamma' red.}$  and  $A_{\gamma'-free}$ ,  $n_{\gamma'-free}$  have to be determined.

There are two boundary conditions to assess the stresses in the respective layers. The first condition, Eq. (5), ensures that the creep rates of  $j$  layers are equal. The second condition confirms that the total force, which acts on the whole structure, can be written as the sum of the forces in each layer (Eq. (6)).

$$\text{I. Condition: } A_1 \cdot \sigma_1^{n_1} = \dots = A_{j-2} \cdot \sigma_{j-2}^{n_{j-2}} = A_{j-1} \cdot \sigma_{j-1}^{n_{j-1}} = A_j \cdot \sigma_j^{n_j}; \quad (5)$$

$$\text{II. Condition: } F_{total} = \sum_{i=1}^j F_i; \quad (6)$$

It results, for a stack with  $j$  layers using conditions (5) and (6), in a system of  $j$  equations. Based on this condition, Eqs. (7) and (8) conclude, for the two-phase centre region, the  $\gamma'$ -reduced layer and the  $\gamma'$ -free layer.

$$\begin{aligned} \sigma_{two-phase} &= \left( \frac{A_{\gamma'-free}}{A_{two-phase}} \cdot \sigma_{\gamma'-free}^{n_{\gamma'-free}} \right)^{\frac{1}{n_{two-phase}}}; \quad \text{and } \sigma_{\gamma' red.} \\ &= \left( \frac{A_{\gamma'-free}}{A_{\gamma' red.}} \cdot \sigma_{\gamma'-free}^{n_{\gamma'-free}} \right)^{\frac{1}{n_{\gamma' red.}}}; \end{aligned} \quad (7)$$

$$F_{total} = \sigma \cdot$$

$$\begin{aligned} A_0 &= \sigma_{\gamma'-free} \cdot 2l_{\gamma'-free}(t) \cdot \frac{A(t)}{l_0} \\ &+ \sigma_{two-phase} \cdot (l(t) - 2l_{\gamma'-free} - 2l_{\gamma' red.}(t)) \cdot \frac{A(t)}{l_0} \\ &+ \sigma_{\gamma' red.} \cdot 2l_{\gamma' red.} \cdot \frac{A(t)}{l_0}; \end{aligned} \quad (8)$$

Insertion of Eq. (7) in Eq. (8) and solving for  $\sigma_{\gamma'-free}$  results in:

This implicit function can be solved numerically. Because the creep tests were conducted with a uniaxial constant load, it is necessary to account for the true stress within the sample, Eq. (10). For the start time  $t = 0$  the stresses in the model are equal to the initial stresses of the experimental creep tests, which are 230 MPa, 270 MPa and 300 MPa.

$$\sigma(t) = \sigma_0 \cdot (1 + \varepsilon(t)); \quad (10)$$

## 4. Results

### 4.1. Structure, composition and morphology of the oxidized samples

The oxidized René N5 samples, shown in Fig. 3, indicate clearly different areas of oxidation: the two-phase centre region, the  $\gamma'$ -free layer and three separated oxide layers. The oxide layers of Fig. 3 and their properties are listed in Table 2. Their compositions are measured by energy dispersive X-ray spectroscopy (EDX) in the scanning electron microscope (SEM).

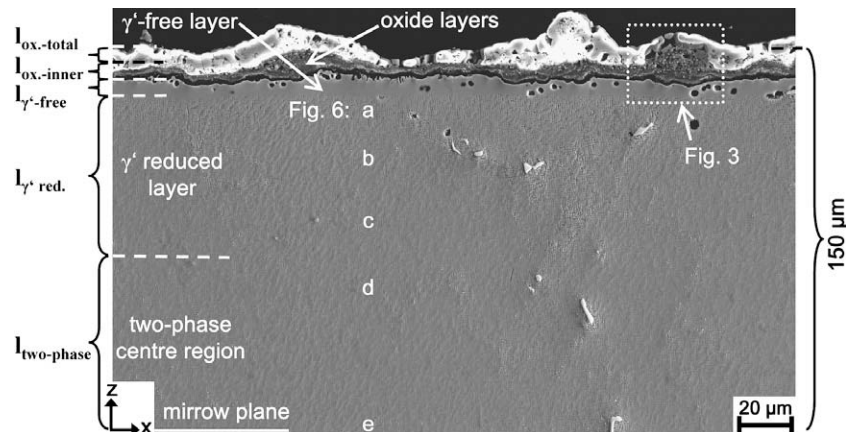


Fig. 2. Scanning electron microscope (SEM) image taken with a secondary electrons (SE) detector of a 0.3 mm thin René N5 sample after stress-free oxidation exposure of 26 h at 980 °C. The marked area on the top right-hand corner is magnified in Fig. 3. The SEM images of the locations (a)–(e) of a 100 h oxidized sample are shown in Fig. 6.

To create the coloured frame, which is printed in Fig. 3 showing the interlayer of oxides, an EDX spectrum of a complete zone has been recorded, in order to identify different phases. Our investigations reveal that the  $\text{Al}_2\text{O}_3$  oxide layer starts to form after an oxidation exposure time of 10 h at 980 °C, whereas the cover oxide layers, NiO and the interlayer of oxides, form immediately after exposure. The interlayer of oxides, which is characterized by a remarkable amount of rhenium ( $\sim 5$  at.%), consists of a spherical phase (Fig. 3b) and a matrix phase (Fig. 3c). The  $\gamma'$ -free layer, which can also be seen in Fig. 3, is characterized by a distinct separation from the  $\gamma'$ -reduced layer and the  $\text{Al}_2\text{O}_3$  oxide layer. Furthermore, pore formation can be seen with increasing oxidation exposure in the  $\gamma'$ -free layer near the oxide layer.

René N5 samples were also oxidized at 1000 °C for 100 h. The mass change was measured and the oxide layers formed were investigated by SEM, EDX and X-ray diffraction (XRD) analysis. The mass gain was less at 1000 °C as compared to 980 °C, indicating that the protective alumina layer forms faster at 1000 °C.

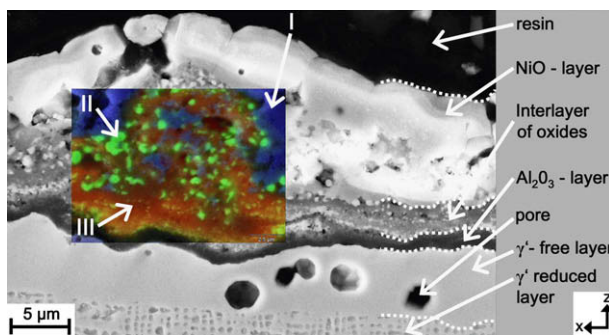


Fig. 3. Scanning electron microscope (SEM) image taken with a QBSD-detector of a 0.3 mm thin René N5 sample after oxidation exposure for 26 h at 980 °C. The coloured frame inside this figure showing the multiphase composition of the interlayer of oxides is generated via energy dispersive X-ray spectroscopy (EDX) in order to identify different phases.

The XRD results, shown in Fig. 4, reveal the formation of different oxides and spinels, namely  $\text{Al}_2\text{O}_3$ , NiO,  $\text{Cr}_2\text{O}_3$ ,  $\text{NiCr}_2\text{O}_4$ ,  $\text{AlTaO}_4$ , and  $\text{NiAl}_2\text{O}_4$ ; some of the species found in the oxide layer formed at 980 °C could not be detected in the layer formed at 1000 °C.

The SEM image of a 1000 °C sample reveals two distinct oxide layers (Fig. 5), instead of three layers, observed at 980 °C (Fig. 3). The inner layer was found to be alumina with some incorporation of Ta, Ni and O, as detected by EDX. The NiO top layer contains Ni, Al, O, Ta and Cr, confirming the presence of the transient oxides detected by XRD.

The two-phase centre region shows with increasing stress-free oxidation exposure time a change in morphology and structure of the  $\gamma'$  precipitates. Fig. 6a–e shows the  $\gamma'$  morphology and structure at different distances  $d_c$  to the mirror plane of a 0.3 mm thick sample, which was oxidized for 100 h. Fig. 6f shows the image of an 1.0 mm thick unoxidized reference sample. Close to the  $\gamma'$ -free

Table 2

Composition and properties of the observed oxide layers,  $\gamma'$ -free and  $\gamma'$ -reduced layer and the two-phase centre region at 980 °C.

Layer number	Layer	Identified phase/ composition	Properties
1	Cover oxide layer	NiO, CoO	Thick and porous monophase layer
2	Interlayer of oxides	$\text{NiAl}_2\text{O}_4$ , $\text{NiTa}_2\text{O}_6$ , $\text{Cr}_2\text{O}_3$	Thick and porous layer consisting of two fractions
3	Third oxide layer	$\text{Al}_2\text{O}_3$	Dense and thin monophase layer
4	$\gamma'$ -free layer	Composition see Table 1	Al-content of 2.2 wt.%, pore formation
5	$\gamma'$ -reduced layer	Composition in-between layer number 4 and 6	Reduced Al content, $\gamma'$ morphology change
6	Two-phase centre region	Nominal composition of René N5 (Table 1)	Regular $\gamma'/\gamma$ structure, see Fig. 6f

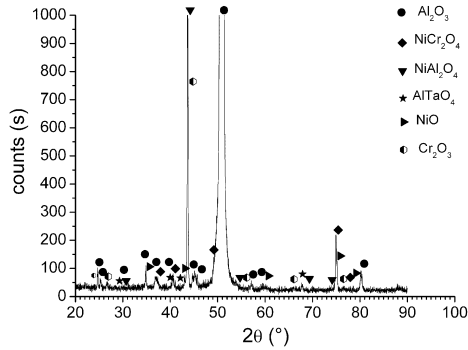


Fig. 4. XRD pattern (Cu anode) of René N5 oxidized in air at 1000 °C for 100 h.

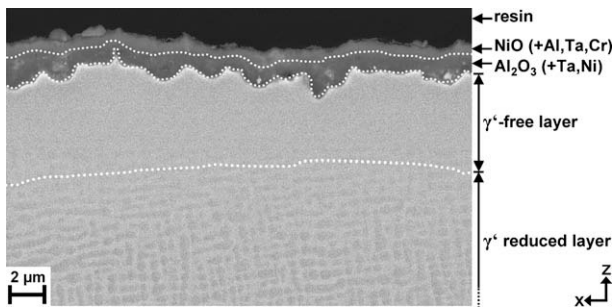


Fig. 5. Cross-section of René N5 after 100 h oxidation in air at 1000 °C.

layer, the  $\gamma'$  precipitates have a spherical morphology (Fig. 6a). This layer is about 25  $\mu\text{m}$  wide, followed by an about 55  $\mu\text{m}$  wide layer in which the  $\gamma'$  precipitates grow together and form a rafted-like structure (Fig. 6b and c). The next layer, 20  $\mu\text{m}$  wide, has a regular structure consisting of enlarged cuboidal precipitates, shown in Fig. 6d. In the centre of the specimen, the  $\gamma'$  phase has a cubic struc-

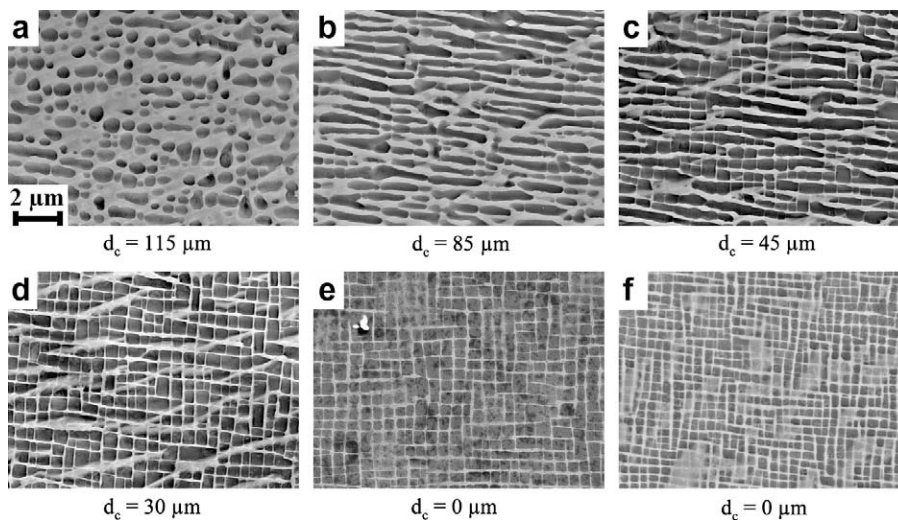


Fig. 6. QBSD-SEM-images (a)–(e) taken at different distances  $d_c$  to the centre of the sample, showing the  $\gamma'$  precipitations of a 0.3 mm thick sample after stress-free oxidation exposure for 100 h at 980 °C. The image (f) shows the  $\gamma'$  structure on the centre ( $d_c = 0$ ) of a 1.0 mm thick unoxidized reference sample.

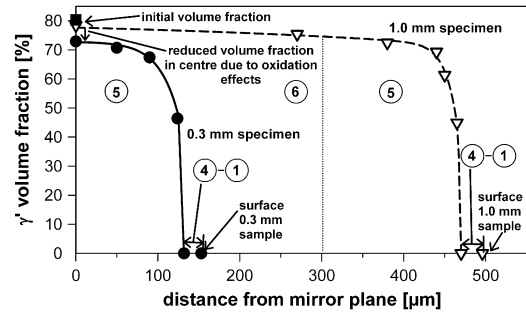


Fig. 7. The volume fraction of the  $\gamma'$  precipitates plotted as a function of the distance from the mirror plane of 100 h oxidized samples at 980 °C. A loss of  $\gamma'$  volume fraction in the centre of the 0.3 mm thick sample due to oxidation effects is observed.

ture (Fig. 6e). The  $\gamma'$  precipitates have coarsened, compared to the  $\gamma'$  morphology of the reference sample (Fig. 6f).

To measure the change in  $\gamma'$  volume fraction, the technique of lineal analysis was performed on SEM images. A 0.3 mm and a 1.0 mm thick sample oxidized for 100 h have been analysed. Fig. 7 shows the measured  $\gamma'$  volume fraction dependent on the distance to the mirror plane of the sample. Fig. 7 indicates that the core of the 0.3 mm thin sample has a 5% reduced  $\gamma'$  volume fraction, compared to the 1.0 mm or to the untreated sample. The unoxidized sample has a  $\gamma'$  volume fraction of about 80%. Due to a scatter of the initial  $\gamma'$  volume fraction of 5% the transition from the two-phase centre layer (layer 6) to the  $\gamma'$ -reduced layer (layer 5) is defined at a  $\gamma'$  volume fraction of 76%. For the 1.0 mm thick oxidized sample, the  $\gamma'$  volume fraction in the core is constant, whereas a 100–150  $\mu\text{m}$  wide region, close to the surface, exhibits a decreased  $\gamma'$  volume fraction. Especially striking is the nearly identical slope close to the surface of both samples. The 0.3 mm sample shows a reduced  $\gamma'$  volume fraction throughout the total cross-

tion. Although the two specimens show different  $\gamma'$  fractions ( $\sim 78\%$  and  $\sim 73\%$ , respectively) in the centre area, they have the same volume fraction of  $\gamma'$  phase ( $\sim 46\%$ ) at the interface to the  $\gamma'$ -free layer.

Furthermore, the oxidation behaviour of the creep samples tested in a vacuum of  $10^{-5}$  mbar and a leakage rate of  $3 \times 10^{-2} \frac{\text{mbar}\cdot\text{l}}{\text{s}}$  has been examined. A first sign of oxide layer formation has been observed after a test time of 330 h. The surface of this vacuum creep sample shows a very slight oxide formation of a  $0.3 \mu\text{m}$  thick NiO single layer. For shorter periods no oxide layer formation has been observed.

#### 4.2. Thermodynamic simulation of the oxidation behaviour

A one-dimensional model is calculated by the software DICTRA [18,20]. The model, schematically drawn in Fig. 8, consists of an area with the nominal composition of René N5, see Table 1, and a surface which is exposed to pure oxygen. Since the first calculations did not converge using the available databases [15,16], the concentration of cobalt has been replaced by the same amount of nickel. Due to a significant shortening of the average calculating time, the small amount of Hf has been replaced by nickel too, see Table 1. During the simulation, the following phases were allowed to form:  $\text{M}_2\text{O}_3$ , MO,  $(\text{AB}_2\text{O}_4)$  and the  $\text{L1}_2$ -ordered  $\gamma'$  phase, where M, A and B describe metal atoms (Al, Cr, Mo, Ni, Re, Ta, W).

In the model, diffusion only takes place in the  $\gamma$  matrix, since the databases [15] are only available for the face-centred cubic (fcc) matrix. This approximation is valid, because diffusion in solid solutions is much faster than in ordered intermetallic phases [19]. The simulation provides

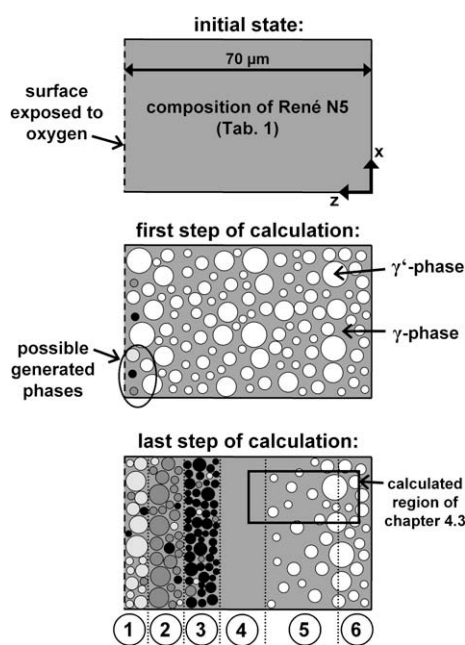


Fig. 8. Schematic illustration of an oxidation behaviour calculating model.

information about the stable phases and their distributions and also about the diffusion path of the elements. A simulation range of  $70 \mu\text{m}$ , duration of 26 h and a temperature of  $980 \text{ }^\circ\text{C}$  at standard pressure were chosen.

The oxidation simulation results are shown in Fig. 9. The mass fractions of the generated phases are plotted versus the distance to the surface, which is exposed to oxygen.

The respective layers, which can be extracted from Fig. 9, are identified by Nos. 1–6. Layer 1 describes the top oxide layer consisting of primary NiO and  $\text{Ni}(\text{Al}, \text{Cr})_2\text{O}_4$ . Layer 2 consists of a mixture of  $\text{Cr}_2\text{O}_3$ ,  $\text{Ni}(\text{Al}, \text{Cr})_2\text{O}_4$ ,  $\text{Al}_2\text{O}_3$  and NiO and the last oxide layer (3) is composed of  $\text{Al}_2\text{O}_3$  and a small amount of  $\text{Cr}_2\text{O}_3$ . In addition to the three oxide layers the  $\gamma'$ -free layer (4) can be identified. In layer 4, a decreasing fraction of  $\text{Al}_2\text{O}_3$  as well as a rising progression of the  $\gamma$  content can be seen. Layer 5, the  $\gamma'$ -reduced layer, is characterized by an increased mass fraction of  $\gamma'$ , which ranges from 0% to 60%. The centre part (6) represents the two-phase centre region, with a constant mass fraction of  $\gamma'$  and  $\gamma$  phase. It should be noted that a high mass fraction of  $\gamma$  matrix is presented in all layers. The  $\gamma$  matrix is necessary in the simulation to enable the mass transport. Due to the simulation set-up a dense non-matrix layer cannot be formed, because a dense layer would stop the diffusion process.

#### 4.3. Growth law simulation of $\gamma'$ -reduced layer by a thermodynamic diffusion couple simulation

The creep-oxidation model is based on time-dependent evolutions of layers with different creep properties. Exact measurement of the width of the  $\gamma'$ -reduced layer  $l_{\gamma' \text{ red.}}$  is difficult and time-consuming, since the  $\gamma'$  volume fraction has to be determined locally. The  $\gamma'$ -reduced layer can be measured indirectly by EDX line scans, because the Al-content of the superalloy declines towards the oxide surface, which results in a reduction of the  $\gamma'$  phase.

Therefore, a one-dimensional diffusion couple was simulated with two areas, called two-phase centre region and  $\gamma'$ -free layer. A schematic drawing of the model is shown in the top left-hand corner of Fig. 10, and was solved by the program DICTRA. The two-phase centre region consists of the nominal composition of René N5, see Table 1.

The average Al-composition of the  $\gamma'$ -free layer is measured by EDX and has been used as a starting value for the  $\gamma'$ -free layer (Table 1). The  $\gamma'$  precipitates were allowed to form in both areas. At the beginning of the simulation  $\gamma'$  precipitates form automatically in the two-phase centre region material. A simulation time of 100 h, a simulation range of  $300 \mu\text{m}$  and a temperature of  $980 \text{ }^\circ\text{C}$  at standard pressure were used. The result of the simulation is shown in Fig. 10, which displays the thickness  $l_{\gamma' \text{ red.}}$  of the  $\gamma'$ -reduced layer against time. The error bars of the simulation data points result from the error-prone measurement of the  $\gamma'$ -reduced layer thickness within the range of the simulation database.

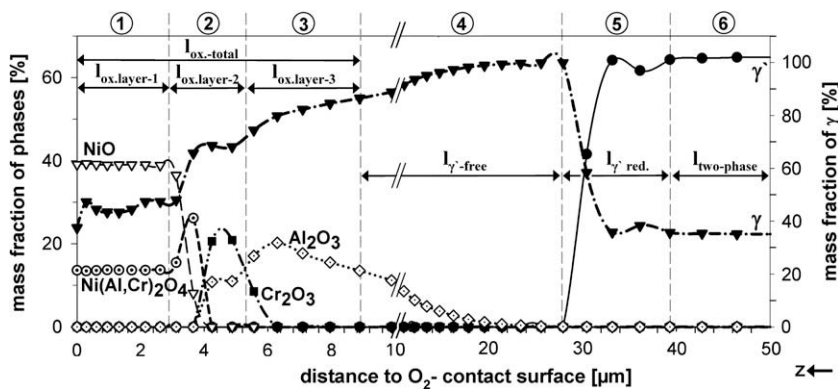


Fig. 9. The result of the oxidation simulation after a simulated time of 26 h. The mass fraction progressions of the generated phases are plotted as a function of the distance to the free surface. Note the different scaling of the  $x$ -axis, which displays the oxide layers with a better resolution.

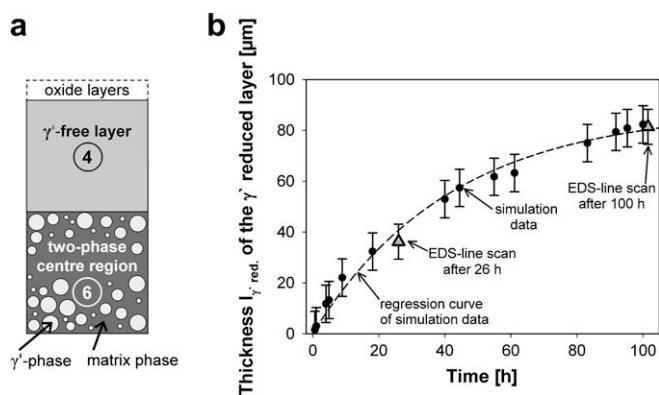


Fig. 10. Growth of the  $\gamma'$ -reduced layer, layer in-between two-phase centre region ((6) in Fig. 9) and  $\gamma'$ -free layer ((4) in Fig. 9). (a) Schematic illustration of a diffusion couple as calculated with DICTRA is shown. The oxide layers are only shown for the sake of completeness; they are not taken into account in the simulation. (b) Thickness determined by thermodynamic simulation and EDX.

In addition to the simulation results two values from EDX measurements after 26 h and 100 h of oxidation are plotted in the diagram, which are in very good agreement with the calculated values. The extracted growth law of the  $\gamma'$ -reduced layer together with the experimentally

observed growth laws of the other layers are shown in Table 3.

#### 4.4. Growth laws and layer positions in dependence of the specimen thickness

For the identification of the growth laws, all oxide layers and the  $\gamma'$ -free layer were measured with the help of optical microscopic pictures and SEM images. Table 3 shows the growth laws with its parameters of layers for the 0.3 mm and 1.0 mm thick samples. Independent of the specimen thickness, both specimen geometries show, with high accuracy, an identical thickness growth of the NiO layer and the interlayer of oxides (layers 1 and 2). The total oxide layer is also measured individually and independent of the three single oxide layers showing a specimen-thickness-independent logarithmic growth behaviour. But the  $\text{Al}_2\text{O}_3$  layer shows a distinct different growth in dependence of the specimen thickness (layer 3 in Table 3). Since the  $\text{Al}_2\text{O}_3$  layer is thin in comparison to the other two oxide layers (layers 1 and 2), a larger fluctuation is given and can explain the variation in thickness of layer 3.

The NiO layer and the interlayer of oxides do not grow parabolic [21] but logarithmic. Using a logarithmic growth law the measured thicknesses of the  $\gamma'$ -free layer can be

Table 3

Growth laws of the oxide layers, the  $\gamma'$ -free and  $\gamma'$ -reduced layers and the two-phase centre region.

Layer number	Layer	Growth law ( $t[h]$ )	Parameters		
1	NiO-layer	$d(t) = a \cdot \ln(t) + b$	$\frac{a_{thin}}{a_{thick}}$	$\frac{b_{thin}}{b_{thick}}$	
2	Interlayer of oxides		1.07	1.09	
			1.04	1.01	
3	$\text{Al}_2\text{O}_3$ -layer	$d(t) = c \cdot \sqrt{t}$	$\frac{c_{thin}}{c_{thick}}$		
			0.59		
4	$\gamma'$ -free layer	$d(t) = e \cdot \ln(t + f) + g$	$\frac{e_{thin}}{e_{thick}}$	$\frac{f_{thin}}{f_{thick}}$	$\frac{g_{thin}}{g_{thick}}$
			0.97	1.03	0.92
			$i \left[ \frac{\mu\text{m}}{\log(t)} \right]$	$j [h]$	$k [\mu\text{m}]$
5	$\gamma'$ -reduced layer	$d(t) = i \cdot \ln(t + j) + k$		12.9	-94.55
6	Two-phase centre region	$d(t) = \frac{l_0}{2} + \xi - \sum_{i=1}^5 d_i(t)$			$\xi = l_{ox-total} - l_{ox-inner}$

approximated with very high accuracy. Within the scatter the coefficients of the  $\gamma'$ -free layer growth law show no dependence on the specimen thickness. The thickness reduction of the two-phase centre region has not been measured, since the thickness reduction can be written as a sum of the thicknesses of each single layer.

Fig. 11 summarizes the determined growth laws, which will be used in the model. The layer locations are given with respect to the position of the initial sample surface. The initial substrate surface position is determined by thermogravimetric analysis and calculations including density and growth behaviour of each layer.

While the width of the two-phase centre region decreases during oxidation, the specimen is getting thicker. About 2/3 of the NiO layer pokes out of the initial substrate surface. The remaining NiO layer expands into the sample. After an oxidation exposure time of 100 h the metal substrate of a 0.3 mm sample reduces about 8% by oxide layer formation. Since we assume the oxide layer  $l_{ox-total}$  as non load-bearing, the load-bearing sample cross-section is reduced by the ratio  $\frac{l_0 - l_{ox-inner}}{l_0}$ .

#### 4.5. Coefficient identification

The identification of the prefactors  $A$  and the stress exponents  $n$  of Eq. (4) for the two-phase centre region can be extracted from vacuum creep curves [8,9]. Parameters for the  $\gamma'$ -free layer are available from creep tests done at single-crystal samples made of single-phase nickel solid solution single crystal with the matrix composition of CMSX-4 [23]. The prefactor  $A$  and stress exponent  $n$  of the  $\gamma'$ -reduced layer are estimated by interpolating the boundary values of the adjacent coefficients. The coefficients used are listed in Table 4. The prefactor of the oxide layers is assumed to be infinity, since these layers are assumed to be not load-bearing within the creep-oxidation model. The primary creep coefficients  $m$  and  $\varepsilon_t$  are also

listed in Table 4. These coefficients are identified using experimental vacuum creep curves [8,9]. Due to the fact that primary creep stage could not be detected for the 0.3 mm thick specimen loaded with an initial stress of 300 MPa, the coefficient  $\varepsilon_t$  is set to zero.

#### 4.6. Results of creep-oxidation model

In Fig. 12 the results of the creep tests and the results of the creep-oxidation model for two specimen thicknesses 0.3 mm and 1.0 mm with varying initial stresses and different atmospheres are illustrated. To compare the measured and calculated creep curves, it is necessary to use different scalings.

All calculated creep-oxidation curves in vacuum simulate the experimental creep behaviour with good accuracy. The vacuum creep curves are calculated by neglecting the growth laws of the oxide layers, the  $\gamma'$ -free layer and  $\gamma'$ -reduced layer. These calculated curves in vacuum assume no change in the load-bearing sample thickness, resulting in a constant strain rate or a constant slope in  $\varepsilon$  versus  $t$  plots.

The calculated curves under air follow the experimental creep curves in the first half of the curve progression very well, since the model merely describes primary and secondary creep stage.

The approximation behaviour for all experimental creep curves is more accurate for the smaller specimen thicknesses and lower initial stresses (Fig. 12a). For higher stresses (Fig. 12c, d and f) the creep tests show a reduced primary and secondary creep stages and start early with tertiary creep. As stated in Section 3, tertiary creep is not handled by our model. Fig. 12f shows that Garofalo equation fits primary creep well. Constant stress versus constant load leads to a slight increase in slope of the calculated curves.

## 5. Discussion

The results of the René N5 oxidation tests conducted at 980 °C are in good agreement with other second-generation Ni-based superalloys [22,32–34]. Investigations of samples, which are stress-free oxidized at 1000 °C, reveal very similar results with the exception of the interlayer of oxides.

The NiO layer (layer 1), the interlayer of oxides (layer 2) and the  $\gamma'$ -free layer (layer 4) extracted from the tests at 980 °C show no dependence on specimen thickness (Table 3). Only the growth law of the  $Al_2O_3$  layer (layer 3) depends on specimen thickness. The thin samples show a reduced growth behaviour of the alumina layer and therefore a lower growth law coefficient  $c$ . Fig. 7 shows a 5% reduced  $\gamma'$  volume fraction of the thinner sample, which indicates a reduction of the aluminium content in the centre of the thin specimen. Although, as long as  $\gamma'$  phase in the specimen cross-section exists, the Al activity in the  $\gamma$  phase is constant, acting as a constant driving force for the Al diffusion, significant differences in the alumina layer

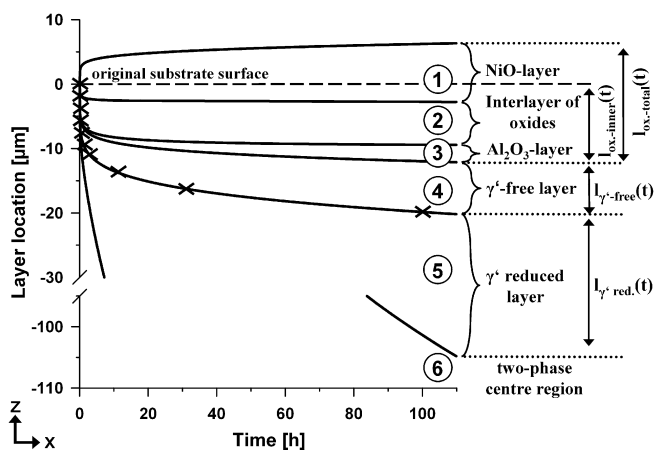


Fig. 11. Growth laws and layer location with respect to the sample surface before oxidation exposure. The layer thicknesses are determined after oxidation exposure of 0, 0.2, 0.5, 0.75, 1, 1.5, 2, 11, 26 and 100 h. Measured points are shown as an example at the boundary from  $\gamma'$ -free layer to  $\gamma'$ -reduced layer.

Table 4

Stress exponents  $n$  and prefactors  $A$  of the different layers and primary creep stage coefficients  $m$  and  $\varepsilon_t$ .

Modelling parameter		Coefficients		Source
Layer				
Two-phase centre region		$n_{two-phase} = 7.4$	$A_{two-phase} = 1.39 \times 10^{-18} \text{ h}^{-1} \text{ MPa}^{-7.4}$	[8,9]
$\gamma'$ -reduced layer		$n_{\gamma' red.} = 11.7$	$A_{\gamma' red.} = 1.25 \times 10^{-23.3} \text{ h}^{-1} \text{ MPa}^{-11.7}$	Interpolated
$\gamma'$ -free layer		$n_{\gamma' free} = 15$	$A_{\gamma' free} = 1.06 \times 10^{-30} \text{ h}^{-1} \text{ MPa}^{-15}$	[23]
Vacuum creep sample				
		$m [\text{s}^{-1}]$	$\varepsilon_t$	
$l_0$ [mm]	$\sigma_0$ [MPa]			
0.3	230	0.46	$7 \times 10^{-4}$	[8,9]
0.3	300	–	0	[8,9]
1.0	230	0.57	$6 \times 10^{-3}$	[8,9]
1.0	300	0.79	$9 \times 10^{-3}$	[8,9]

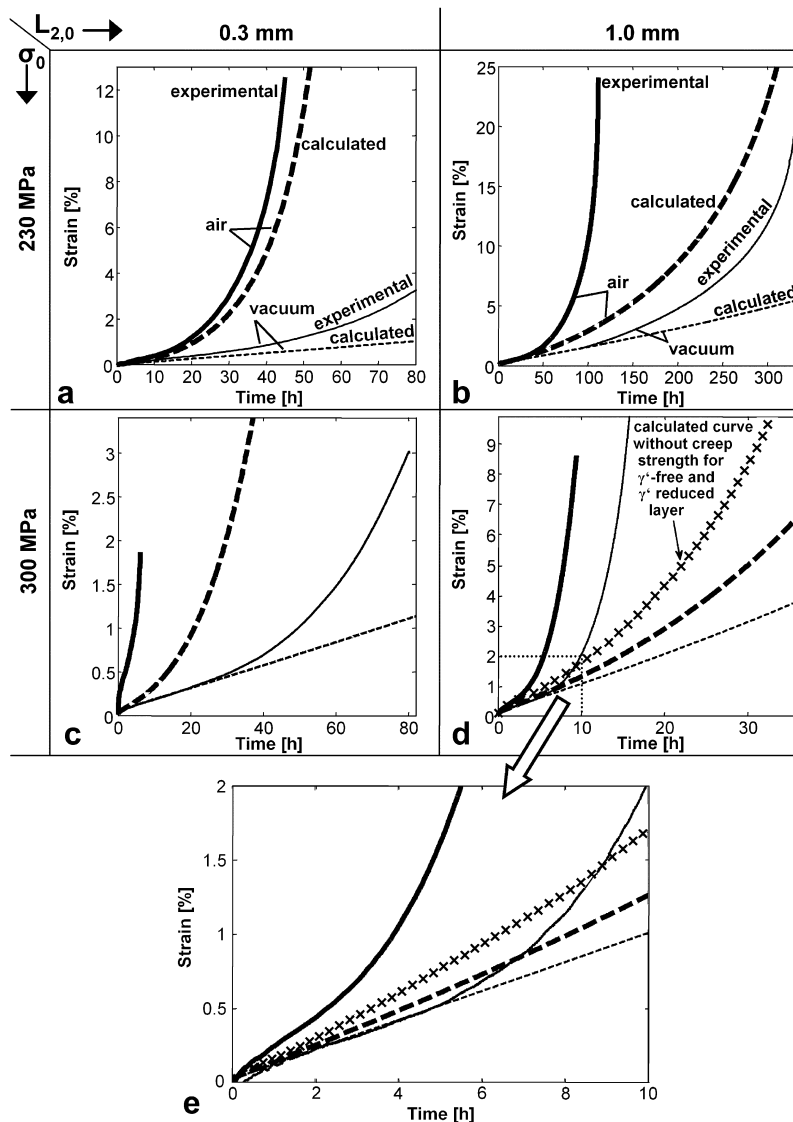


Fig. 12. Curve progressions of creep tests (solid lines) and calculated creep-oxidation curves (dashed lines) of two specimen geometries (left 0.3 mm, right 1.0 mm), two stress levels (upper part lower stress lower part higher stress) and in different media (thick in air, thin in vacuum). The crossed curve in (d) and (e) shows simulated curve with zero creep strength for all exterior layers (oxide,  $\gamma'$ -free and  $\gamma'$ -reduced layer). (e) shows the magnified primary creep behaviour of (d) up to 10 h. Note the different scaling for each graph.

growth process have been observed. A reason for the thickness-dependent alumina growth is the stronger influence of oxide layer stresses on microstructure of thin specimens.

These proportional higher stresses result in an increased microstructure change of the  $\gamma'$  phase, acting as a diffusion barrier. Based on this effect, rafted  $\gamma'$  structures are formed

parallel to the substrate surface. An earlier raft formation was observed for thinner specimens, see Fig. 6b, which hinders the Al diffusion towards the surface. This results in a lower alumina growth law coefficient  $c$  of the thin specimens. Further investigation will be carried out to further analyse the specimen-thickness-dependent alumina growth behaviour.

Fig. 13 is based on the results of Table 3 and of Figs. 7 and 11. Under constant test conditions ( $t = 100$  h;  $T = 980$  °C), the relation between the alumina growth law coefficient  $c$  and the elongation change of the  $\gamma'$ -reduced layer (layer 5) as well as the two-phase centre region (layer 6) is dependent on the initial specimen thickness  $l_0$ . The thickness ranges from 2.0 mm down to 0.2 mm. The curves for 2.0 mm and 0.2 mm are extrapolated from the 0.3, 0.4 and 1.0 mm data.

The  $\gamma'$ -reduced layer and the two-phase centre region offer different precipitation volume fractions. The  $\gamma'$  containing layers (layer 5 and 6) are defined in  $x$ -direction by the ordinate and the dashed line and the curve, and in  $y$ -direction by the zero-line and the curve. The factor  $e$  is an indicator of the existence of the two-phase centre region (layer 6) and the width of the  $\gamma'$ -reduced layer (layer 5). Therefore, an initial specimen thickness can be determined in which the two-phase centre region (layer 6) does not exist. This happens for an about 0.4 mm thick specimen marked by an arrow in Fig. 13a. For samples  $l_0 > 0.4$  mm the  $\text{Al}_2\text{O}_3$  growth law coefficient remains a constant value  $c_{ss}$ . The results of Table 3 are indicated by two crosses in Fig. 13a.

Moreover, an aluminium depletion should have a big influence on the creep behaviour under air only for small specimen thicknesses or/and cyclic temperature profiles [30]. Calvarin-Amiri et al. [31] show the load-dependent oxidation behaviour of the Ni alloy Ni–Cr20. Since stresses existing within the sample cross-section are able to influence the oxide growth, the differences in oxidation and

creep behaviour in dependence of the specimen thickness indicate a different state of stresses between the thick and thin samples. Further investigation will be carried out in this context.

In contrast to the logarithmic growth law of the total oxide layer, Raffaitin et al. [32] detected a parabolic oxide mass gain of MC2 samples, which have been exposed at 1150 °C up to 700 h. Strong oxidation effects should be observed for longer times and thinner samples. This is reflected very well by the comparison of experiment and simulation in Fig. 12.

A very good agreement exists between the experimental investigations (Section 4.1) and the values of a thermodynamic oxidation simulation using DICTRA (see Section 4.2. and Fig. 9). Since diffusion is allowed in the fcc phase only, the generated oxides do not form a dense oxide layer, in contrast to the experiments. The curve progression of each calculated oxide layer shows a broad transition zone on both sides of the maximum. Although the oxidation behaviour has to be approximated, the stacking sequence as well as the characteristic curve progression of each experimental observed layer can be calculated in high accuracy. During the investigation of the  $\gamma'$ -reduced layer a very good agreement exists between the regression curve based on kinetic and thermodynamic simulations (Section 4.3) and the measured values analysed by EDX line scans (Fig. 10). A similar distribution of the aluminium content is measured in Ref. [32] using EDX line scans of oxidized samples of MC2.

The curves for 0.3 mm thick specimens at low stress (230 MPa) calculated by the creep-oxidation model are in very good agreement with the experimental creep curves. The discrepancies between simulation and experiment at 300 MPa and 1.0 mm specimen thickness can be explained by the onset of tertiary creep, which is not handled in our model. The effects of this creep stage dominate the experimental behaviour of thin as well as thick samples at high stresses ( $\geq 270$  MPa) and therefore the deviation between calculation and experiment increases.

An additional simulation has been carried out for 300 MPa and 1.0 mm specimen thickness in air. In this simulation all layers, except the two-phase centre region, are assigned to have zero creep strength. This calculated curve is indicated by cross-symbols in Fig. 12d. The experimental behaviour in air within the primary creep regime (up to 3 h test time) is represented very well, whereas the secondary and soon-beginning tertiary creep is deviating strongly. Even with the assumption of zero creep strength to all layers except the centre region, the calculated creep behaviour is weaker than the measured creep curve under air. This is an indication for additional effects acting on the two-phase centre region, such as  $\gamma'$  reduced volume fraction and/or rafting and/or  $\gamma'$  coarsening, which is not covered by our model.

A change in the  $\gamma'$ -morphology was noticed during the analyses of the oxidized samples. This effect will be considered in subsequent studies by a structure-dependent pre-exponential factor  $A_{\gamma' \text{ red.}}$  and a structure-dependent stress

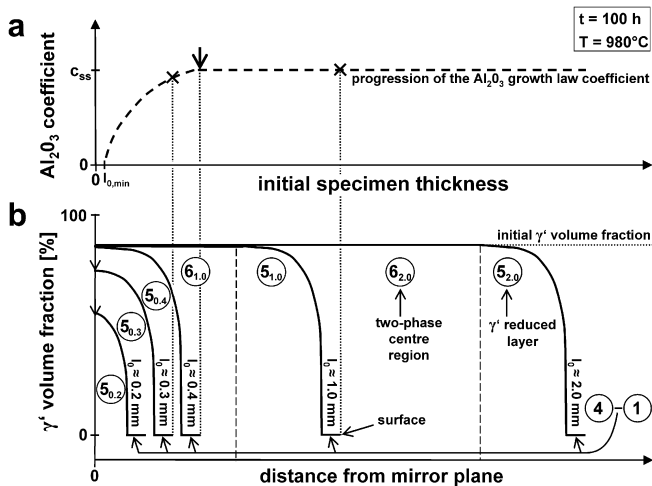


Fig. 13. Schematic curve progressions at constant test conditions (a) displays the  $\text{Al}_2\text{O}_3$  growth law coefficient  $c$  in dependence of the initial specimen thickness  $l_0$ . The  $\gamma'$  precipitation volume fraction of different initial specimen thicknesses in dependence of the distance from the mirror plane shows (b).

exponent  $n_{\gamma' red.}$ , because structure, morphology, volume fraction, size and coarsening of the  $\gamma'$  precipitates strongly influence creep behaviour [24–29,33].

The good approximation of the real creep curves with the creep-oxidation model of samples with 0.3 mm thickness shows that oxidation is an important factor for the creep behaviour in thin samples, at low stresses and long creep times.

## 6. Summary

A model which describes the influence of oxidation on the creep behaviour for thin-walled structures is presented.

- Oxidation was determined in stress-free oxidation exposure of single-crystal René N5 samples at 980 °C (Table 2).
- Growth laws of oxides, of the  $\gamma'$ -reduced layer and of the  $\gamma'$ -free layer were presented (Table 3).
- The  $Al_2O_3$  growth law coefficients (Table 3) give information about the existence of the two-phase centre region as well as the width of the  $\gamma'$ -reduced layer (Fig. 13).
- The two-phase centre region of the 0.3 mm specimen shows an Al depletion indicated by a reduced  $\gamma'$  volume fraction (Fig. 7).
- Sequence and characteristics of the experimentally observed layers could be reproduced via kinetic and thermodynamic calculations.
- Excellent agreement exists between the one-dimensional thermodynamic simulation of the  $\gamma'$ -reduced layer and the experimental results using EDX line scans (Fig. 10).
- Combined creep-oxidation behaviour was modelled using these creep parameters for each layer and respective growth laws.
- The comparison of the oxidation-creep model with creep experiments (Fig. 12) shows that with 0.3 mm thick specimens and low stress of 230 MPa, the accuracy of the model is very good, whereas tertiary creep is dominating the creep behaviour in thick samples and high stresses, which is not included in the model. Oxidation strongly influences the creep properties of thin ( $\approx 0.3$  mm) specimens at low stresses ( $\approx 230$  MPa).
- Due to the occurrence of stresses below 100 MPa and thicknesses below 1 mm in a turbine blade application, it is extremely important to consider the influence of oxidation effects on the creep behaviour of thin-walled structures.

## References

- [1] Nabarro FRN, De Villiers HL. The physics of creep: creep and creep-resistant alloys. London: Taylor & Francis; 1995.
- [2] Kofstad P. Oxid Met 1995;44:1–2.
- [3] Bürgel R. Mater Sci Technol 1986;2:302–8.
- [4] Dryepondt S, Monceau D, Crabos F, Andrieu E. Acta Mater 2005;53:4199–209.

- [5] Don M, Heckler A. SAE Technical Paper 851785. Warrendale: Society of Automotive Engineers Inc.; 1985.
- [6] Doner M, Heckler JA. Identification of mechanisms responsible for degradation in thin-wall stress rupture properties. In: Duhl DN, Maurer G, Antolovich S, Lund C, Reichman S, editors. Superalloys. Warrendale: TMS; 1988. p. 653.
- [7] Seetharaman V, Cetel AD. Thickness debit in creep properties of PWA 1484. In: Green KA, Pollock TM, Harada H, Howson TE, Reed RC, Schirra JJ, et al., editors. Superalloys. Seven Springs: TMS; 2004. p. 207.
- [8] Hüttner R, Völkl R, Gabel J, Glatzel U. Creep behavior of thick and thin walled structures of a single crystal nickel-base superalloy at high temperatures – experimental method and results. In: Reed RC, Kenneth KA, Caron P, Gabb TP, Fahrman MG, Huron ES, et al., editors. Superalloys. Warrendale: TMS; 2008. p. 719.
- [9] Hüttner R, Gabel J, Glatzel U, Völkl R. Mater Sci Eng, A 2009;510–511:307–11.
- [10] Wu CS, Buchakjian L. Improved property-balanced nickel-based superalloy for producing single crystal articles. UK patent application GB 2 235 697 A; 1991.
- [11] Th Version TCCR, ThermoCalc Software AB, Stockholm, Sweden; 2006. <<http://www.thermocalc.com>>.
- [12] DICTRA Version 24, ThermoCalc Software AB, Stockholm, Sweden; 2006. <<http://www.thermocalc.com/Products/Dicttra.html>>.
- [13] Garofalo F. ASTM special technical publication 1960;283:82.
- [14] Garofalo F. Fundamentals of creep and creep rupture in metals. New York: Macmillan; 1965.
- [15] TCS Ni-alloys Mobility Database, MOBNI1, Version 1.0, ThermoCalc Software AB, Stockholm, Sweden; 2006.
- [16] Thermotech Ni-based Superalloys Database, TTNI7, Version 7.0, ThermoCalc Software AB, Stockholm, Sweden; 2006.
- [17] Norton FH. The creep of steel at high temperatures. New York: MCGraw-Hill; 1929.
- [18] Borgenstam A, Engstrom A, Hoglund L, Ågren A. J Phase Equilib 2000;21:269–80.
- [19] Engström A, Morral J, Ågren J. Acta Mater 1997;45:1189–99.
- [20] Andersson JO, Helander T, Hoglund L, Shi PF, Sundman B. Calphad 2002;26:273.
- [21] Young D. High temperature oxidation and corrosion of metals. In: Burstein T, editor. Elsevier corrosion series, vol. 1. Amsterdam: Elsevier; 2008.
- [22] Akhtar A, Hedge S, Reed RC. JOM 2006;58:37–42.
- [23] Knobloch C, Sass V, Siebörger D, Glatzel U. Mater Sci Eng 1997;A234:237–41.
- [24] Caron P, Ramusat C, Diologent F. Influence of the  $\gamma'$  fraction on the  $\gamma/\gamma'$  topological inversion during high temperature creep of single crystal superalloys. In: Reed RC, Kenneth KA, Caron P, Gabb TP, Fahrman MG, Huron ES, et al., editors. Superalloys. Warrendale (USA): TMS; 2008. p. 159.
- [25] Kondo Y, Kitazaki N, Namekata J. Effect of morphology of  $\gamma'$  phase on creep resistance of a single crystal nickel-based superalloy CMSX-4. In: Kissinger RD, Deye DJ, Anton DL, Cetel AD, editors. Superalloys. Seven Springs/Pa: TMS; 1996. p. 297.
- [26] Mukherji D, Rösler J. Zeitsch Metall 2003;94:478–84.
- [27] Lvova E, Norsworthy D. J Mater Eng Perform 2001;10:299–313.
- [28] Erricson GL. The development and application of CMSX<sup>®</sup>-10. In: Kissinger RD, Deye DJ, Anton DL, Cetel AD, editors. Superalloys. Seven Springs/Pa: TMS; 1996. p. 35.
- [29] Karunaratne MSA, Carter P, Reed C. Mater Sci Eng 2000;281:229–35.
- [30] Orosz R, Krupp U, Christ HJ, Monceau D. Oxid Met 2007;68:165–76.
- [31] Calvarin-Amiri G, Molins R, Huntz AM. Oxid Met 2000;54:399–426.
- [32] Raffaitin A, Monceau D, Andrieu E, Crabos F. Acta Mater 2006;54:4473–87.
- [33] Pfennig A, Fedelich B. Corros Sci 2008;50:2484–92.
- [34] Younes CM, Allen GC, Nicholson JA. Corros Eng, Sci Technol 2007;42:80–8.